How do normal faults grow above dykes?

Craig Magee[1] (c.magee@leeds.ac.uk), Christopher A-L Jackson[2] (c.jackson@imperial.ac.uk)

[1]Institute of Geophysics and Tectonics, School of Earth Science and Environment, University of Leeds, Leeds, LS2 9JT, UK

[2]Basins Research Group, Department of Earth Science and Engineering, Imperial College London, London, SW7 2BP, UK

This manuscript is a non-peer reviewed pre-print submitted to EarthArXiv. The manuscript has not been submitted yet.

How do normal faults grow above dykes?

Craig Magee[1]*, Christopher A-L Jackson[2]

[1]Institute of Geophysics and Tectonics, School of Earth Science and Environment, University of Leeds, Leeds, LS2 9JT, UK

[2]Basins Research Group, Department of Earth Science and Engineering, Imperial College London, London, SW7 2BP, UK

*corresponding author: c.magee@leeds.ac.uk

Dykes feed volcanic eruptions and drive crustal extension on Earth and other planetary bodies. Yet many dykes stall at depth, inducing normal faulting of overlying rocks. Whilst dyke-induced faults provide a surficial record of dyking, unlocking these archives is difficult because we do not know how they grow above or geometrically relate to dykes in 3D. Here we use seismic reflection images to quantify the 3D structure and kinematic history of dyke-induced faults for the first time. We show variations in fault dip and displacement distribution control the surface expression of dyke-induced faults. Discrete fault segments nucleated between the dyke upper tip and surface during phases of lateral dyke propagation, whilst periods of dyke stalling and thickening prompted fault segment growth and linkage. Our results demonstrate at-surface measurements of dyke-induced fault (e.g. heave and graben half-width) cannot be used to estimate dyke parameters (e.g. thickness and upper tip depth) without a priori knowledge of fault kinematics. We show reflection seismology is a powerful tool for studying how normal faults grow above dykes, and anticipate future seismic-based

studies will improve our understanding of dyke emplacement and its translation into surface deformation.

Geodetic and seismicity data confirm dyke intrusion can induce normal faulting of overlying rocks in various volcano-tectonic settings (Wright et al., 2012; Passarelli et al., 2015; Sigmundsson et al., 2015; Xu et al., 2016). Dyke-induced normal faults, henceforth dyke-induced faults, typically form planar, conjugate pairs that dip in towards underlying dykes and bound dyke-parallel graben (Fig. 1) (Pollard et al., 1983; Mastin and Pollard, 1988; Rubin, 1992; Rowland et al., 2007; Trippanera et al., 2015a; Hjartardóttir et al., 2016b; Al Shehri et al., 2018). The growth and geometry of these dyke-induced faults and graben, coupled with associated seismicity and/or broader ground deformation, reflects dyke emplacement mechanics and shape (Pollard et al., 1983; Rubin and Pollard, 1988; Pallister et al., 2010; Dumont et al., 2016; Dumont et al., 2017). For example, extension (heave) across dyke-induced faults at the surface is considered a proxy for dyke thickness (Rubin and Pollard, 1988), whilst other structural parameters (e.g. graben length and half-width) are used to estimate dyke length, height, and upper tip depth (Pollard et al., 1983; Wilson and Head, 2002; Hjartardóttir et al., 2016a). Our understanding of how faults grow above dykes dictates how we relate fault properties and deformation signals (e.g. seismicity) to dyke geometry, and therefore underpins: (i) tracking intruding dykes by monitoring fault activity (Pallister et al., 2010); (ii) determining whether dyke-induced faults will inhibit (Maccaferri et al., 2016) or promote (Rivalta and Dahm, 2004) dyke ascent and eruption; (iii) establishing how dyke-induced faults influence rift zone topography (Pollard et al., 1983; Rubin, 1992) and instigate volcano flank instability (McGuire, 1996); (iv) accurately estimating dyke volumes to assess melting conditions and magma supply (Wilson and Head, 2002); and (v) evaluating the role of dykes in planetary processes (e.g. continental break-up (Wright et al., 2012; Ruch et al., 2016; Dumont et al., 2017) and seafloor spreading (Carbotte et al., 2006)) on Earth and other planetary bodies. However, because we can only observe the surface expression of natural dyke-induced faults, how they kinematically and, thus, geometrically relate to underlying dykes remains poorly understood.

Physical, analytical, and numerical models supplement our understanding of how faults grow above dykes by providing 2D cross-sectional, and occasionally 3D, views of these systems (Pollard et al., 1983; Mastin and Pollard, 1988; Trippanera et al., 2015b; Hardy, 2016). Yet there remains no consensus on the vertical extent of dyke-induced faults or whether they nucleate: (i) as vertical fractures at the surface, where tensile stress concentrates, before propagating downwards as faults towards the dyke tip (Fig. 1a) (Acocella et al., 2003; Trippanera et al., 2015a; Trippanera et al., 2015b; Al Shehri et al., 2018); (ii) immediately above the dyke tip in areas of tension, before propagating upwards and perhaps breaching the surface (Fig. 1b) (Grant and Kattenhorn, 2004; Xu et al., 2016); (iii) a combination of (i) and (ii), with both segments growing towards each other and perhaps linking (Fig. 1c) (Tentler, 2005; Rowland et al., 2007); (iv) between the dyke tip and surface, propagating upwards and downwards with continued slip (Fig. 1d) (Mastin and Pollard, 1988); or (v) in front of a laterally propagating dyke, eventually being cross-cut by the dyke (Fig. 1e) (Rubin and Pollard, 1988; Rowland et al., 2007). These five hypotheses only describe dyke-induced fault kinematics in cross-section (i.e. in 2D), but can be used to predict displacement-depth trends (Fig. 1); i.e. displacement is typically greatest where faults nucleate (Walsh and Watterson, 1988). Our simple displacement-depth predictions show the nucleation site(s) of dyke-induced faults controls their surface properties (e.g. heave), which are only directly comparable to dyke parameters if fault initiation occurred at the surface (Fig. 1a) (Trippanera et al., 2015b). Constraining dyke parameters and emplacement mechanics thus requires us to unravel the geometry and kinematics of dyke-induced faults.

However, field observations, seismicity, and geodetic data are insufficient to unequivocally determine where dyke-induced faults nucleate; e.g. seismicity reveals faulting can occur anywhere between the dyke tip and surface (Ukawa and Tsukahara, 1996; Passarelli et al., 2015; Ágústsdóttir et al., 2016), but not whether earthquakes correspond to nucleation or reactivation of faults (Rubin and Pollard, 1988).

Recognition of dykes and dyke-induced faults in seismic reflection data (Bosworth et al., 2015) means we can finally examine their 3D structure and test how faults relate geometrically and kinematically to underlying dykes. Using 2D and 3D seismic data from the Exmouth Plateau, offshore NW Australia (Fig. 2a), we identify a previously unrecognised swarm of NE-striking dykes (the Exmouth Dyke Swarm) emplaced within the Triassic clastic rocks of the Mungaroo Formation. The dykes manifest as planar, >9–1.5 km high, up to >79 km long, <300 m wide, low-amplitude zones that disrupt otherwise sub-horizontal stratigraphic reflections (Figs 2b-d). We interpret these low-amplitude zones as dykes, or packages of closely spaced dykes (Wall et al., 2010; Phillips et al., 2017), because they: (i) occur across multiple seismic surveys with different processing histories, implying they are not geophysical artefacts (Fig. 2d) (Phillips et al., 2017); (ii) cross-cut but do not laterally offset channels, indicating they are not strike-slip faults (e.g. Fig. 2d); and (iii) appear similar to vertical dykes inferred in other seismic datasets (Wall et al., 2010; Bosworth et al., 2015).

Above and parallel to the dykes are NE-trending, ~1–2 km wide graben bound by low-displacement (i.e. <150 m), conjugate normal faults. These faults offset a ~1 km thick Triassic-to-Early Cretaceous clastic-dominated sequence, including amalgamated Valanginian-to-Hauterivian unconformities at their upper tips, which we infer represented the seabed during faulting (Figs 2b, c, e) (Exon et al., 1982; Reeve et al., 2016). Individual faults are continuous or visibly segmented along-strike and dip inwards (on average at ~45°) to converge at the upper tips of underlying dykes (Figs 2b, c, e); the faults do not intersect dyke walls (cf. Rubin and Pollard, 1988). We suggest dyking triggered formation of these faults, based on their spatial relationship to inferred dykes and plan-view similarity (i.e. linear, long, and low-displacement) to dyke-induced faults observed in Afar (Rowland et al., 2007; Dumont et al., 2016; Dumont et al., 2017), Iceland (Bull et al., 2003; Hjartardóttir et al., 2016a), Egypt (Bosworth et al., 2015), and those recreated using different modelling approaches (Mastin and Pollard, 1988; Trippanera et al., 2015b; Hardy, 2016). Cross-cutting of Valanginian-to-Hauterivian unconformities by the dyke-induced faults indicate faulting, and thus dyke emplacement, occurred in the Early Cretaceous, coincident with break-up of the NW Australian margin (Exon et al., 1982; Reeve et al., 2016) and voluminous magmatism (Symonds et al., 1998).

To understand how faults grow above dykes, we quantify fault properties across an ~18 km long section of a graben bound by two dyke-induced faults (i.e. F1 and F2) and examine their relationship to the geometry and emplacement mechanics of an underlying dyke or dykes (Fig. 3). Subtle but abrupt changes in strike of the broadly N-trending dyke(s) occur along its length, sub-dividing it into segments with trends of 007°, 014°, and 004°; the northernmost dyke segment extends for >5 km beyond the seismically resolved portion of the faults (Fig. 3a). The top of the dyke(s), onto which F1 and F2 converge, is located at a current depth of ~3.5±0.25 km (Figs 2c, 3d). The width of the low-amplitude zone marking the dyke(s), which probably does not correspond to true or cumulative dyke thickness (Wall et al., 2010) but can be considered as a proxy for relative thickness trends, gradually decreases northwards from ~250 m to ~100 m (Figs 3a, d). In the south of the study area, the dyke(s) extends below the survey limit, but dyke height appears to decrease northwards in a step-wise manner from >5 km to ~1.7 km as the depth to the dyke(s) base apparently decreases (Fig. 3d). This apparent decrease in the width and height of the dykes geophysical expression suggest they propagated laterally from south to north.

Graben half-width, a proxy for a dykes proximity to the surface (Pollard et al., 1983; Trippanera et al., 2015b; Hjartardóttir et al., 2016a), ranges from ~366–728 m and is typically less than the depth to the dykes upper tip by up to ~470 m (Figs 3d, e). Graben half-width and dyke upper tip depth are only weakly positively correlated (Fig. 3e) because fault dip varies, from ~20–65°, across the dyke-induced faults (i.e. they are not planar; Fig. 3c, f). Displacement also varies along-strike and down-dip of both F1 and F2 (displacement maximum of ~73 m and ~158 m, respectively; Fig. 3b). Zones of high displacement (e.g. S1-S4 on F2), separated by displacement minima, are observed along F1 and F2; e.g. S4 is ~2.7 km long (Fig. 3b). The transition between S3 and S4 occurs above a change in dyke trend from 007° to 014° (Figs 3a, b). For the same equivalent along-strike position, displacement on both faults commonly differs, with F2 primarily accommodating more offset (Fig. 3b). Cumulative heave across both F1 and F2 is up to ~105 m and broadly decreases northwards, consistent with a reduction in the width of the low-amplitude zone marking the dyke(s) (Fig. 3d). Changes in heave across zones of high-displacement are up to ~82 m (i.e. S1; Fig. 3b). Displacement-depth profiles are complex but occasionally display clear 'M-shaped' or 'C-shaped' trends (Muraoka and Kamata, 1983); displacement maxima rarely occur at the lower tips of F1 and F2 and never at their upper tips (Figs 3a, f). The 3D distribution of high displacement zones across F1 and F2 suggests fault growth via linkage of discrete, but potentially kinematically coherent slip surfaces (i.e. fault segments) (Tentler and Mazzoli, 2005; Dumont et al., 2017), which nucleated between the dyke(s) upper tip and contemporaneous surface (Mastin and Pollard, 1988), with strain partitioned onto F2.

Dyke-induced faulting is kinematically linked to dyke emplacement (Pollard et al., 1983), implying observed segmentation of fault displacement and heave (Fig. 3b) (Tentler and Mazzoli, 2005; Dumont et al., 2017) probably corresponds to along-strike changes in dyke parameters, particularly thickness. Spatial variations in dyke thickness can be driven by segmentation during dyke propagation, linkage of dyke segments (i.e. step and broken bridge formation), and/or localised inelastic deformation (e.g. fluidisation or thermal erosion) of the wall rock (Delaney and Pollard, 1981; Gudmundsson, 1983; Kavanagh and Sparks, 2011; Daniels et al., 2012; Gudmundsson et al., 2012; Rivalta et al., 2015; Vachon and Hieronymus, 2017; Magee et al., 2018). Quantitative analyses along individual dykes reveal thickness changes related to inelastic wall rock deformation are typically less than a few tens of metres and occur over metres to several hundred metres (Pollard and Muller, 1976; Gudmundsson, 1983; Kavanagh and Sparks, 2011; Daniels et al., 2012). Because our fault heave data suggests dyke thickness varies by up to ~82 m over ~2–3 km (Fig. 3), and dyking can broadly be described by elastic processes (Rivalta et al., 2015), we consider inelastic deformation has a negligible impact on dyke thickness and fault displacement at the scale of our study (Pollard et al., 1983). We therefore favour dyke segmentation as a mechanism for generating discrete, laterally separated fault segments along the length of a dyke (Fig. 4).

We propose propagation of bladed dyke segments (Rubin, 1995; Townsend et al., 2017; Healy et al., 2018) promotes nucleation and rapid lengthening of an overlying fault (Fig. 4a). Because a critical dyke thickness is required to instigate faulting (Trippanera et al., 2015b), we expect fault nucleation and, thus, areas of high displacement to develop over the thickest (and highest) section of dyke blade (Fig. 4a) (Trippanera et al., 2015b). Dyke blades thin towards their propagating edge (Rubin, 1995; Townsend et al., 2017; Healy et al., 2018), implying faults will be shorter than the dyke and their displacement will decrease laterally (Fig. 4a) (Trippanera et al., 2015a). These predicted dyke-fault relationships are supported by extension of the studied dyke beyond the low-displacement, northern limits of F1 and F2 (Figs 2 and 3), where cessation of dyking has preserved the relationship between fault segment evolution and dyke propagation. We suggest new, isolated fault segments can be produced when a new, bladed dyke segment propagates from the nose of a stalled dyke (Fig.

4c). During the 2014 Bárðarbunga dyking event, frequent stalling of the laterally intruded dyke led to pressure build-up behind its tip, until the energy barrier inhibiting intrusion was overcome and a new dyke segment propagated (Sigmundsson et al., 2015; Woods et al., 2019). Such periods of stalling and pressurization may be expected to promote dyke thickening (Sigmundsson et al., 2015; Trippanera et al., 2015b), inducing slip on overlying faults. Stalling may also be characterised by crystallisation of dyke margins, particularly towards its upper tip where the host rocks are coolest (Fig. 4b). Given the bladed geometry of the lateral dyke tip, and potential crystallisation around its margins, we suggest magma supplying renewed propagation will be channelized, breaking-out from the dyke nose to feed a new bladed segment (Fig. 4c) (Healy et al., 2018). New dyke segments propagate quickly (Sigmundsson et al., 2015), but the thickest and highest section of a bladed segment in our conceptual model will be situated along-strike from the necking zone connecting it to the main dyke (Fig. 4c). New dyke-induced normal faults will therefore nucleate above the new bladed dyke segment, along-strike from existing faults (Fig. 4c). Inflation of the new bladed dyke segment, including the necking zone connecting it to the preceding dyke, will promote growth and linkage of dyke-induced fault segments (Fig. 4d). Displacement minima mark where faults linked; these zones thus likely overlie sites where the leading edge of laterally propagating dykes stalled (Fig. 4d). The occurrence of a displacement minima between S3 and S4 above a change in dyke strike (Figs 3a, b), and our inference this marks a zone where the leading dyke edge stalled, is consistent with observations from the Bárðarbunga showing dyke segments have subtly different orientations (Sigmundsson et al., 2015; Woods et al., 2019).

We confirm dyke-induced faults extend from the contemporaneous surface and converge on, but do not continue below, the dykes upper tip (cf. Rubin and Pollard, 1988; Rowland et al., 2007). The dyke-induced faults we studied nucleated between the dyke and contemporaneous seabed (Mastin and Pollard, 1988), contrasting with many proposed models that state dyke-induced faults nucleate at the surface and/or upper dyke tip (Pollard et al., 1983; Rubin and Pollard, 1988; Acocella et al., 2003; Grant and Kattenhorn, 2004; Tentler, 2005; Rowland et al., 2007; Trippanera et al., 2015a; Trippanera et al., 2015b; Xu et al., 2016; Al Shehri et al., 2018). Our kinematic reconstruction implies seismicity generated by this type of dyke-induced faulting is likely to be concentrated away from the dyke upper tip in areas where faults nucleate and accrue the most slip, primarily when dyke propagation has stalled and thickening occurs. Our results also indicate cumulative heave measured along the contemporaneous surface would not equal dyke thickness (cf. Rubin and Pollard, 1988). Furthermore, we demonstrate dyke-induced fault dip varies along-strike and down-dip, implying dyke upper tip depths estimated from graben half-width, which commonly assume faults are planar, may be incorrect (cf. Pollard et al., 1983; Mastin and Pollard, 1988; Rubin and Pollard, 1988; Trippanera et al., 2015a; Hjartardóttir et al., 2016a). To accurately constrain dyke geometry (e.g. thickness, depth, and volume) from the surface expression of dyke-induced faults thus requires knowledge of where the faults nucleated and their 3D geometry; unfortunately this information is commonly unavailable. Using seismic reflection data to unravel how faults grow above dykes and quantify their 3D structure can improve our understanding of dyke emplacement and its role in driving crustal extension (e.g. continental break-up) on Earth and other planetary bodies.

Methods

Seismic reflection data

The Glencoe and Chandon 3D, time-migrated seismic reflection surveys have a bin spacings of 25 m and record lengths of 8 s two-way time (TWT) and 6 s TWT, respectively. The Chandon survey is displayed with an SEG negative polarity; i.e. a trough (black) reflection corresponds to a downward increase in acoustic impedance whilst a peak (white) reflection represents a downward decrease in acoustic impedance. The Glencoe survey is displayed with an SEG positive polarity. To constrain dyke between the two 3D seismic datasets we used 2D seismic lines from the Champagne 2D MSS and JA95 surveys.

Dyke imaging

Dykes are rarely directly imaged (i.e. expressed as a discrete reflection) in seismic reflection data because their sub-vertical orientation means little energy is reflected back to and recorded at the surface (Thomson, 2007). The dykes we describe, similar to those inferred in the North Sea by Wall et al. (2010), are rather expressed by an absence or reduction in imaging; i.e. less energy is reflected from the stratigraphic horizons where they are intersected by dykes, meaning their lateral continuity is disrupted. Changes to the mechanical properties of wall rock adjacent to dykes by contact metamorphism of the wall rock will also influence energy reflection, thereby increasing the width of the low-amplitude zones of zones centred on the dykes (Wall et al., 2010). The geophysical expression of the dykes is, thus, technically a vertical seismic artefact, the width of which does not necessarily correspond to dyke thickness (Wall et al., 2010). However, we suggest that relative changes in the width of the low-amplitude zones of disruption along-strike mimic relative variations in dyke thickness. The observed northwards thinning of the low-amplitude zones marking the dyke and a northwards decrease in heave, another proxy for dyke thickness (Rubin and Pollard, 1988), supports our inference that the geophysical expression of the dykes can be related to their geometry.

Borehole data

Eight boreholes were used to tie mapped horizons between the datasets and determine their age: Mercury-1, Yellowglen-1, Chandon-1, Chandon-2, Chandon-3, Toporoa-1, Nimblefoot-1, and Cloverhill-1 (Fig. 2). To depth-convert the Chandon 3D survey around the studied dyke-induced faults and the upper dyke tips, we used checkshot and horizon depth data from Mercury-1, Yellowglen-1, Chandon-2, and Chandon-3 (Supplementary Table 1). Specifically, we calculated interval velocities between the seabed, Top Muderong Formation, Top Mungaroo Formation, and down to 4 s TWT; we assumed a velocity of 1.5 km s^{-1} for the water column. Conversion of dyke base depth measurements from s TWT to metres, which occurs below the limits of our depth-conversion, was conducted by extrapolating a second order polynomial trend-line through the cumulative checkshot data of the five wells (Supplementary Table 1).

Seismic Resolution

Between the top of the dyke-induced faults (~2.9 s TWT or ~2.6 km) and the approximate middle of the dykes (~4.5 s TWT; ~5.3 km), we used velocity data defined from the boreholes and measurements of average dominant frequency across three inlines to calculate the vertical and horizontal resolution of the data; the base of the dyke-induced faults occurring at ~3.5 s TWT or ~3.5 km. We specifically define the vertical resolution as the limits of separability (λ/4, where λ is the seismic wavelength) and visibility (λ/30); i.e. the minimum thickness of a layer where reflections from its top and base can be distinguished defines the limit of separability (Brown, 2004). The limit of visibility defines the thickness at which a layer can be distinguished from background noise in the seismic reflection data (Brown, 2004). A layer with a thickness between the limits of separability and visibility is characterised by a tuned reflection package, created when reflections from its top and base interfere on their way to the surface and cannot be deconvolved (Brown, 2004).

We measured the dominant frequency and interval velocity for every 0.1 s TWT increments, from 2.8–4.5 s TWT, to quantify changes in resolution with depth (Supplementary Table 2). To account for potential variability in interval velocities, which may arise due to human error or lateral changes in lithology away from the boreholes, we consider interval velocities have ±10% errors (Supplementary Table 2). We show the data resolution broadly decreases with depth (Supplementary Table 2). For the strata hosting the dyke-induced normal faults, the minimum and maximum limits of separability are ~14 m and 29 m, respectively; the average limits of separability and visibility are ~20 m and ~3 m, respectively (Supplementary Table 2).

Quantitative analysis

We selected faults F1 and F2 for displacement distribution analysis because they are continuous along-strike and their northernmost lateral tips are captured in the seismic reflection data. Compared to other dyke-induced normal faults, which are segmented, show subtle curvature along-strike, and/or interact with highly oblique tectonic normal faults, F1 and F2 appear to represent the simplest faults (Fig. 1e).

Eleven sedimentary horizons (i.e. horizons HA–HK; Fig. 1c) from different structural levels were mapped locally around F1 and F2 and their hanging wall and footwall cut-offs were mapped as points every 125 m along-strike. For each cut-off pair, we measured fault throw and extracted fault dip information; this data was used to calculate heave and displacement (Supplementary Table 3). Because the maximum fault heave is a proxy for dyke thickness (Rubin and Pollard, 1988), plots of heave variation along-strike (i.e. Fig. 3d) use the maximum heave on any given vertical transect along-strike; i.e. neighbouring heave data-points may not have been measured on the same horizon. Graben width was measured every 125 m along-strike on Horizon HF; although this horizon does not mark the top of the fault, it is the uppermost prominent reflection that F1 and F2 displace along their entire lengths. Dyke tip depths, used to calculate dyke height, and width of the dykes geophysical expression were measured every 250 m along-strike.

Acknowledgements

CM is funded by a NERC Independent Research Fellowship (NE/R014086/1); CM also acknowledges funding from an Imperial College Research Fellowship. We are grateful to Geoscience Australia for making all data used in this study publically available (http://www.ga.gov.au/nopims). Schlumberger are thanked for provision of Petrel seismic interpretation software.

Figure captions

Figure 1: Different hypotheses for where faults nucleate during dyke propagation: **a,** at the surface (Acocella et al., 2003; Trippanera et al., 2015a; Trippanera et al., 2015b; Al Shehri et al., 2018); **b,** at the dyke tip (Grant and Kattenhorn, 2004; Xu et al., 2016); **c,** at the surface and dyke tip (Tentler, 2005; Rowland et al., 2007); **d,** between the surface and dyke tip (Mastin and Pollard, 1988); or **e,** in front of a laterally propagating dyke (Rubin and Pollard, 1988; Rowland et al., 2007). Expected changes in horizontal stresses (i.e. negative are tensile and positive are compressive) around an intruding dyke are shown for **a-d** (Rubin and Pollard, 1988). We also predict depth-displacement trend predictions for each model.

Figure 2: Dykes and dyke-induced faults imaged in seismic reflection data (see Supplementary Fig. S1 for uninterpreted version and Supplementary Fig. S2 for data video). **a,** Study area location. **b,** Time-migrated seismic section in two-way time (TWT). See **e,** for location. **c,** Depth-converted seismic section, which is vertically exaggerated (VE), showing

horizons used to measure displacement. See **b,** for location. **d,** Root-mean squared (RMS) amplitude extraction across a ~0.1 s TWT high window (see **b,** for location). Well locations marked (1 = Mercury-1; 2 = Chandon-2; 3 = Chandon-1; 4 = Chandon-3; 5 = Yellowglen-1; 6 = Cloverhill-1; 7 = Toporoa-1; 8 = Nimblefoot-1). Inset: RMS amplitude map of Intra-Mungaroo horizon (see **b,**). **e,** Horizon HF time-structure map.

Figure 3: Map-views and quantitative measurements of a dyke and dyke-induced faults (i.e. F1 and F2). **a,** RMS window extraction of dyke (see Fig. 2d). **b,** 3D displacement distribution of F1 and F2. Average limits of separability (L.o.S) and visibility (L.o.V) incorporated into colour-bar. **c,** Dip map of F1 and F2. **d,** Dyke height, tip depth, and apparent thickness, as well as graben half-width and maximum fault heave, plotted against distance. **e,** Graben half-width plotted against depth of upper dyke tip below Horizon HF. **f,** Graben half-width plotted against average dip for F1 and F2 along corresponding vertical transect. **g,** Depth-displacement profiles for F1 and F2. See **b,** for location.

Figure 4: Conceptual model for how dyke segmentation promotes nucleation, growth, and linkage of discrete fault segments.

References

Acocella, V., Korme, T., and Salvini, F., 2003, Formation of normal faults along the axial zone of the Ethiopian Rift: Journal of Structural Geology, v. 25, no. 4, p. 503-513.

Ágústsdóttir, T., Woods, J., Greenfield, T., Green, R. G., White, R. S., Winder, T., Brandsdóttir, B., Steinthórsson, S., and Soosalu, H., 2016, Strike-slip faulting during the 2014 Bárðarbunga-Holuhraun dike intrusion, central Iceland: Geophysical Research Letters, v. 43, no. 4, p. 1495-1503.

Al Shehri, A., Gudmundsson, A. J. J. o. V., and Research, G., 2018, Modelling of surface stresses and fracturing during dyke emplacement: Application to the 2009 episode at Harrat Lunayyir, Saudi Arabia, v. 356, p. 278-303.

Bosworth, W., Stockli, D. F., and Helgeson, D. E., 2015, Integrated outcrop, 3D seismic, and geochronologic interpretation of Red Sea dike-related deformation in the Western

Desert, Egypt–The role of the 23Ma Cairo "mini-plume": Journal of African Earth Sciences, v. 109, p. 107-119.

Brown, A. R., 2004, Interpretation of three-dimensional seismic data, Oklahoma, USA, AAPG and SEG, AAPG Memoir 42, SEG Investigations in Geophysics No. 9, 534 p.:

Bull, J., Minshull, T., Mitchell, N., Thors, K., Dix, J., and Best, A., 2003, Fault and magmatic interaction within Iceland's western rift over the last 9 kyr: Geophysical Journal International, v. 154, no. 1, p. F1-F8.

Carbotte, S. M., Detrick, R. S., Harding, A., Canales, J. P., Babcock, J., Kent, G., Van Ark, E., Nedimovic, M., and Diebold, J., 2006, Rift topography linked to magmatism at the intermediate spreading Juan de Fuca Ridge: Geology, v. 34, no. 3, p. 209-212.

Daniels, K. A., Kavanagh, J. L., Menand, T., and R. Stephen, J. S., 2012, The shapes of dikes: Evidence for the influence of cooling and inelastic deformation: Geological Society of America Bulletin, v. 124, no. 7-8, p. 1102-1112.

Delaney, P. T., and Pollard, D. D., 1981, Deformation of host rocks and flow of magma during growth of minette dikes and breccia-bearing intrusions near Ship Rock, New Mexico: USGPO, 2330-7102.

Dumont, S., Klinger, Y., Socquet, A., Doubre, C., and Jacques, E., 2017, Magma influence on propagation of normal faults: Evidence from cumulative slip profiles along Dabbahu-Manda-Hararo rift segment (Afar, Ethiopia): Journal of Structural Geology, v. 95, p. 48-59.

Dumont, S., Socquet, A., Grandin, R., Doubre, C., and Klinger, Y., 2016, Surface displacements on faults triggered by slow magma transfers between dyke injections in the 2005–2010 rifting episode at Dabbahu–Manda–Hararo rift (Afar, Ethiopia): Geophysical Journal International, v. 204, no. 1, p. 399-417.

Exon, N., Von Rad, U., and Von Stackelberg, U., 1982, The geological development of the passive margins of the Exmouth Plateau off northwest Australia: Marine Geology, v. 47, no. 1-2, p. 131-152.

Grant, J. V., and Kattenhorn, S. A., 2004, Evolution of vertical faults at an extensional plate boundary, southwest Iceland: Journal of Structural Geology, v. 26, no. 3, p. 537-557.

Gudmundsson, A., 1983, Form and dimensions of dykes in eastern Iceland: Tectonophysics, v. 95, no. 3-4, p. 295-307.

Gudmundsson, A., Kusumoto, S., Simmenes, T. H., Philipp, S. L., Larsen, B., and Lotveit, I. F., 2012, Effects of overpressure variations on fracture apertures and fluid transport: Tectonophysics, v. 581, p. 220-230.

Hardy, S., 2016, Does shallow dike intrusion and widening remain a possible mechanism for graben formation on Mars?: Geology, v. 44, no. 2, p. 107-110.

Healy, D., Rizzo, R., Duffy, M., Farrell, N. J., Hole, M. J., and Muirhead, D., 2018, Field evidence for the lateral emplacement of igneous dykes: Implications for 3D mechanical models and the plumbing beneath fissure eruptions: Volcanica, v. 1, no. 2, p. 20.

Hjartardóttir, Á. R., Einarsson, P., Gudmundsson, M. T., and Högnadóttir, T., 2016a, Fracture movements and graben subsidence during the 2014 Bárðarbunga dike intrusion in Iceland: Journal of Volcanology and Geothermal Research, v. 310, p. 242-252.

Hjartardóttir, Á. R., Einarsson, P., Gudmundsson, M. T., Högnadóttir, T. J. J. o. V., and Research, G., 2016b, Fracture movements and graben subsidence during the 2014 Bárðarbunga dike intrusion in Iceland, v. 310, p. 242-252.

Kavanagh, J., and Sparks, R. S. J., 2011, Insights of dyke emplacement mechanics from detailed 3D dyke thickness datasets: Journal of the Geological Society, v. 168, no. 4, p. 965-978.

Maccaferri, F., Rivalta, E., Passarelli, L., and Aoki, Y., 2016, On the mechanisms governing dike arrest: Insight from the 2000 Miyakejima dike injection: Earth and Planetary Science Letters, v. 434, p. 64-74.

Magee, C., Muirhead, J., Schofield, N., Walker, R. J., Galland, O., Holford, S., Spacapan, J., Jackson, C. A., and McCarthy, W., 2018, Structural signatures of igneous sheet intrusion propagation: Journal of Structural Geology.

Mastin, L. G., and Pollard, D. D., 1988, Surface deformation and shallow dike intrusion processes at Inyo Craters, Long Valley, California: Journal of Geophysical Research: Solid Earth, v. 93, no. B11, p. 13221-13235.

McGuire, W. J., 1996, Volcano instability: a review of contemporary themes, *in* McGuire, W. J., Jones, A. P., and Neuberg, J., eds., Volcano Instability on the Earth and Other Planets, Volume 110, Geological Society, London, Special Publications, p. 1-23.

Muraoka, H., and Kamata, H., 1983, Displacement distribution along minor fault traces: Journal of Structural Geology, v. 5, no. 5, p. 483-495.

Pallister, J. S., McCausland, W. A., Jónsson, S., Lu, Z., Zahran, H. M., El Hadidy, S., Aburukbah, A., Stewart, I. C., Lundgren, P. R., and White, R. A., 2010, Broad accommodation of rift-related extension recorded by dyke intrusion in Saudi Arabia: Nature Geoscience, v. 3, no. 10, p. 705.

Passarelli, L., Rivalta, E., Cesca, S., and Aoki, Y., 2015, Stress changes, focal mechanisms, and earthquake scaling laws for the 2000 dike at Miyakejima (Japan): Journal of Geophysical Research: Solid Earth, v. 120, no. 6, p. 4130-4145.

Phillips, T. B., Magee, C., Jackson, C. A.-L., and Bell, R. E., 2017, Determining the three-dimensional geometry of a dike swarm and its impact on later rift geometry using seismic reflection data: Geology, v. 46, no. 2, p. 119-122.

Pollard, D. D., Delaney, P. T., Duffield, W. A., Endo, E. T., and Okamura, A. T., 1983, Surface deformation in volcanic rift zones: Tectonophysics, v. 94, no. 1-4, p. 541-584.

Pollard, D. D., and Muller, O. H., 1976, The effect of gradients in regional stress and magma pressure on the form of sheet intrusions in cross section: Journal of Geophysical Research, v. 81, no. 5, p. 975-984.

Reeve, M. T., Jackson, C. A. L., Bell, R. E., Magee, C., and Bastow, I. D., 2016, The stratigraphic record of prebreakup geodynamics: Evidence from the Barrow Delta, offshore Northwest Australia: Tectonics, v. 35, no. 8, p. 1935-1968.

Rivalta, E., and Dahm, T., 2004, Dyke emplacement in fractured media: application to the 2000 intrusion at Izu islands, Japan: Geophysical Journal International, v. 157, no. 1, p. 283-292.

Rivalta, E., Taisne, B., Bunger, A., and Katz, R., 2015, A review of mechanical models of dike propagation: Schools of thought, results and future directions: Tectonophysics, v. 638, p. 1-42.

Rowland, J., Baker, E., Ebinger, C., Keir, D., Kidane, T., Biggs, J., Hayward, N., and Wright, T., 2007, Fault growth at a nascent slow-spreading ridge: 2005 Dabbahu rifting episode, Afar: Geophysical Journal International, v. 171, no. 3, p. 1226-1246.

Rubin, A. M., 1992, Dike-induced faulting and graben subsidence in volcanic rift zones: Journal of Geophysical Research: Solid Earth, v. 97, no. B2, p. 1839-1858.

Rubin, A. M., 1995, Propogation of magma-filled cracks: Annual Review of Earth and Planetary Sciences, v. 23, p. 49.

Rubin, A. M., and Pollard, D. D., 1988, Dike-induced faulting in rift zones of Iceland and Afar: Geology, v. 16, no. 5, p. 413-417.

Ruch, J., Wang, T., Xu, W., Hensch, M., and Jónsson, S., 2016, Oblique rift opening revealed by reoccurring magma injection in central Iceland: Nature communications, v. 7, p. 12352.

Sigmundsson, F., Hooper, A., Hreinsdóttir, S., Vogfjörd, K. S., Ófeigsson, B. G., Heimisson, E. R., Dumont, S., Parks, M., Spaans, K., and Gudmundsson, G. B., 2015, Segmented lateral dyke growth in a rifting event at Bárðarbunga volcanic system, Iceland: Nature, v. 517, no. 7533, p. 191.

Symonds, P. A., Planke, S., Frey, O., and Skogseid, J., 1998, Volcanic evolution of the Western Australian Continental Margin and its implications for basin development: The Sedimentary Basins of Western Australia 2: Proc. of Petroleum Society Australia Symposium, Perth, WA.

Tentler, T., 2005, Propagation of brittle failure triggered by magma in Iceland: Tectonophysics, v. 406, no. 1, p. 17-38.

Tentler, T., and Mazzoli, S., 2005, Architecture of normal faults in the rift zone of central north Iceland: Journal of Structural Geology, v. 27, no. 9, p. 1721-1739.

Thomson, K., 2007, Determining magma flow in sills, dykes and laccoliths and their implications for sill emplacement mechanisms: Bulletin of Volcanology, v. 70, no. 2, p. 183-201.

Townsend, M. R., Pollard, D. D., and Smith, R. P., 2017, Mechanical models for dikes: a third school of thought: Tectonophysics, v. 703, p. 98-118.

Trippanera, D., Acocella, V., Ruch, J., and Abebe, B., 2015a, Fault and graben growth along active magmatic divergent plate boundaries in Iceland and Ethiopia: Tectonics, v. 34, no. 11, p. 2318-2348.

Trippanera, D., Ruch, J., Acocella, V., and Rivalta, E., 2015b, Experiments of dike-induced deformation: Insights on the long-term evolution of divergent plate boundaries: Journal of Geophysical Research: Solid Earth, v. 120, no. 10, p. 6913-6942.

Ukawa, M., and Tsukahara, H., 1996, Earthquake swarms and dike intrusions off the east coast of Izu Peninsula, central Japan: Tectonophysics, v. 253, no. 3-4, p. 285-303.

Vachon, R., and Hieronymus, C. F., 2017, Effect of host-rock rheology on dyke shape, thickness and magma overpressure: Geophysical Journal International, v. 208, no. 3, p. 1414-1429.

Wall, M., Cartwright, J., Davies, R., and McGrandle, A., 2010, 3D seismic imaging of a Tertiary Dyke Swarm in the Southern North Sea, UK: Basin Research, v. 22, no. 2, p. 181-194.

Walsh, J. J., and Watterson, J., 1988, Analysis of the relationship between displacements and dimensions of faults: Journal of Structural Geology, v. 10, no. 3, p. 239-247.

Wilson, L., and Head, J. W., 2002, Tharsis-radial graben systems as the surface manifestation of plume-related dike intrusion complexes: Models and implications: Journal of Geophysical Research: Planets, v. 107, no. E8.

Woods, J., Winder, T., White, R. S., and Brandsdóttir, B., 2019, Evolution of a lateral dike intrusion revealed by relatively-relocated dike-induced earthquakes: The 2014–15 Bárðarbunga–Holuhraun rifting event, Iceland: Earth and Planetary Science Letters, v. 506, p. 53-63.

Wright, T. J., Sigmundsson, F., Pagli, C., Belachew, M., Hamling, I. J., Brandsdóttir, B., Keir, D., Pedersen, R., Ayele, A., and Ebinger, C., 2012, Geophysical constraints on the dynamics of spreading centres from rifting episodes on land: Nature Geoscience, v. 5, no. 4, p. 242-250.

Xu, W., Jónsson, S., Corbi, F., and Rivalta, E., 2016, Graben formation and dike arrest during the 2009 Harrat Lunayyir dike intrusion in Saudi Arabia: Insights from InSAR, stress calculations and analog experiments: Journal of Geophysical Research: Solid Earth, v. 121, no. 4, p. 2837-2851.

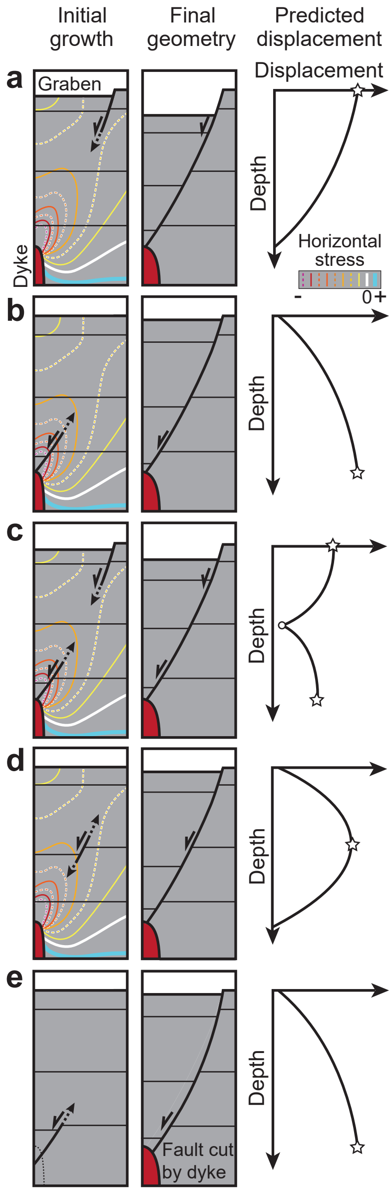

Initial growth
Final geometry
Predicted displacement
a
Graben
Dyke
Displacement
Depth
Horizontal stress
-
0+
b
Depth
c
Depth
d
Depth
e
Depth
Fault cut by dyke

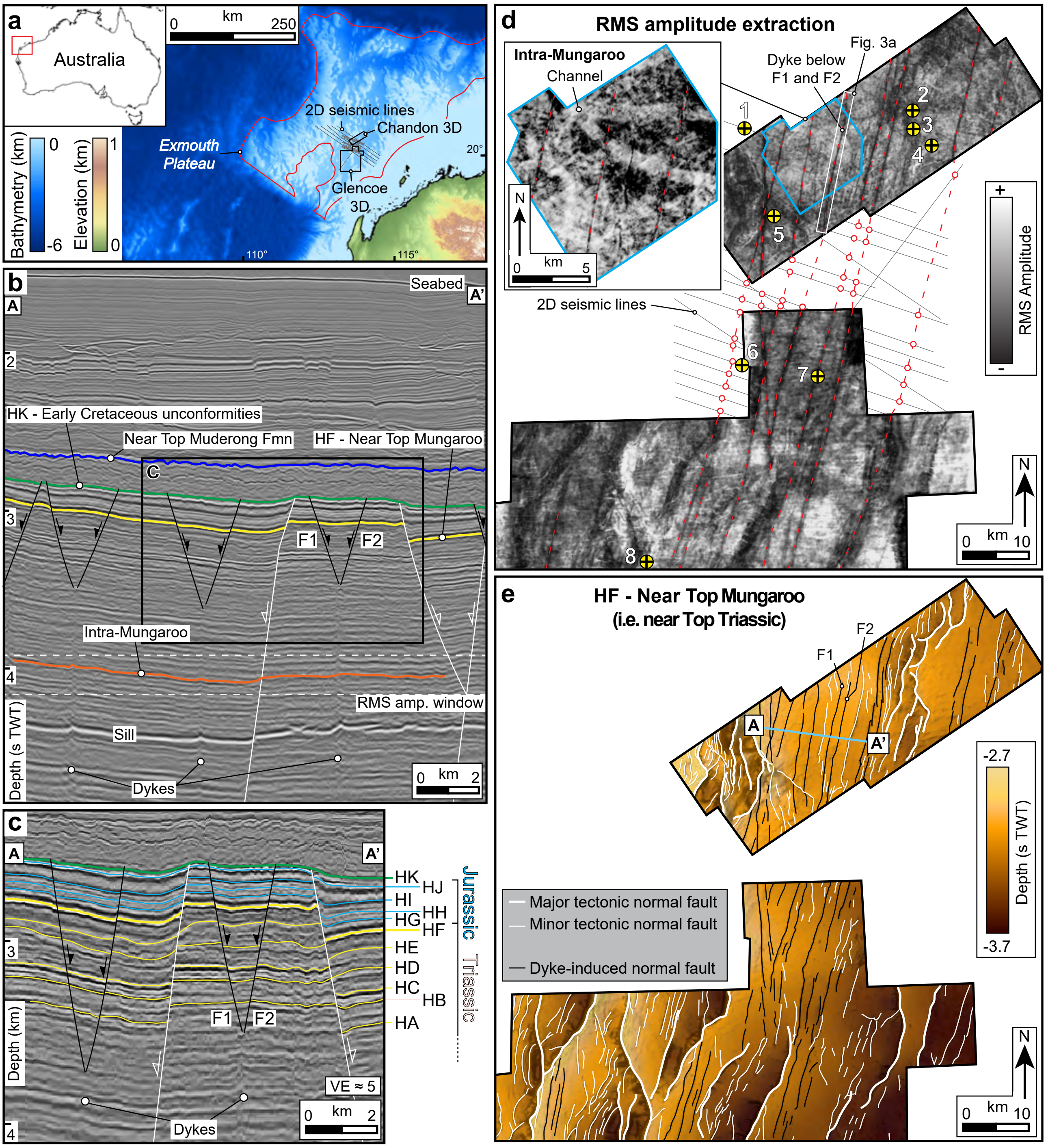
a
Australia
0 km 250
Bathymetry (km)
Elevation (km)
Exmouth Plateau
2D seismic lines
Chandon 3D
Glencoe 3D
20°
110°
115°
b
Seabed
A
A'
HK - Early Cretaceous unconformities
Near Top Muderong Fmn
HF - Near Top Mungaroo
C
F1
F2
Intra-Mungaroo
RMS amp. window
Sill
Dykes
Depth (s TWT)
0 km 2
c
HK
HJ
HI
HH
HG
HF
HE
HD
HC
HB
HA
Jurassic
Triassic
F1
F2
Depth (km)
VE ≈ 5
Dykes
0 km 2
d
RMS amplitude extraction
Intra-Mungaroo
Channel
Fig. 3a
Dyke below F1 and F2
2D seismic lines
RMS Amplitude
0 km 5
0 km 10
e
HF - Near Top Mungaroo
(i.e. near Top Triassic)
F1
F2
A
A'
Depth (s TWT)
-2.7
-3.7
Major tectonic normal fault
Minor tectonic normal fault
Dyke-induced normal fault
0 km 10

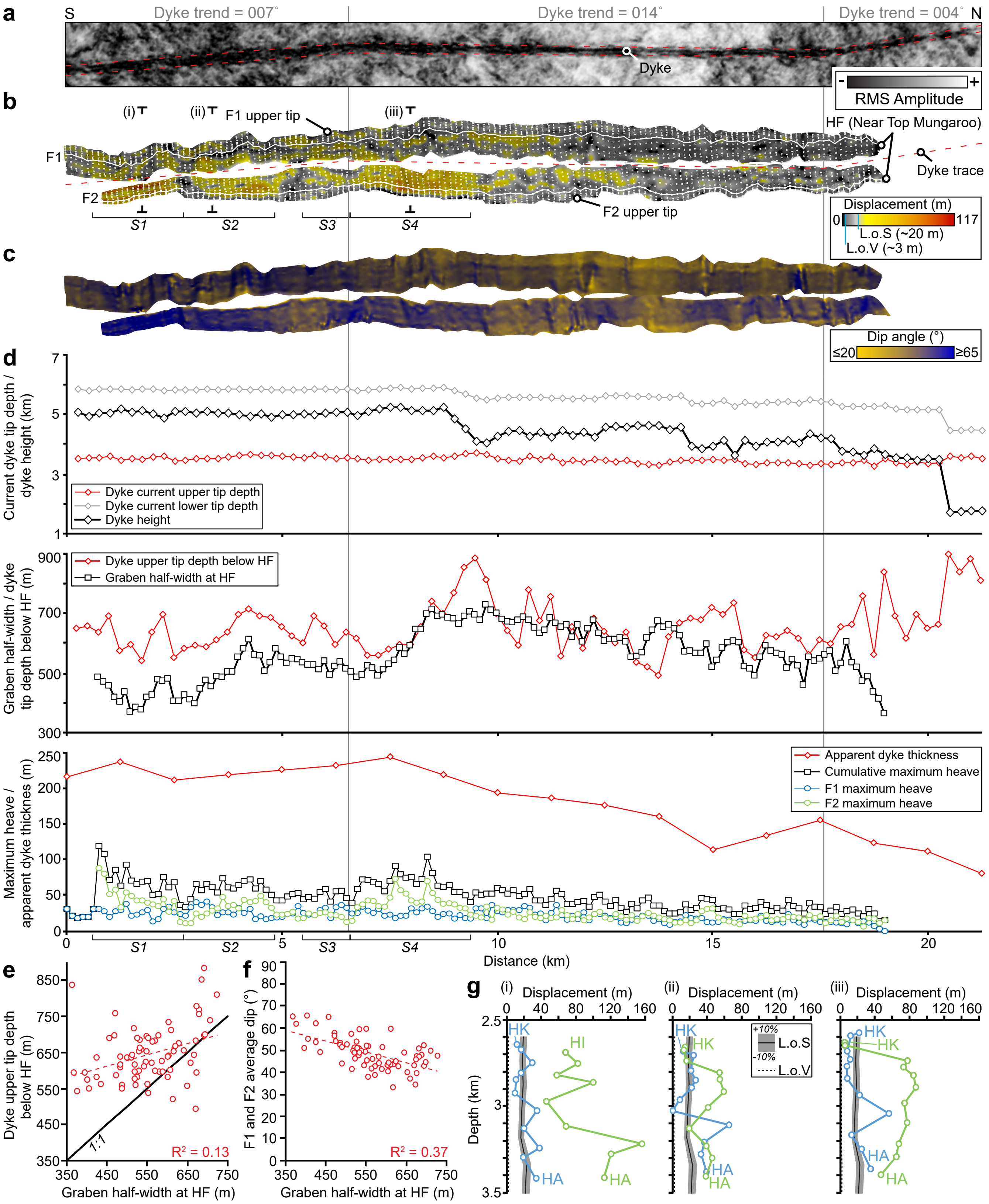

a
S
Dyke trend = 007°
Dyke trend = 014°
Dyke trend = 004°
N
Dyke
RMS Amplitude
b
(i)
(ii)
(iii)
F1 upper tip
F1
F2
HF (Near Top Mungaroo)
Dyke trace
F2 upper tip
S1
S2
S3
S4
Displacement (m)
0
117
L.o.S (~20 m)
L.o.V (~3 m)
c
Dip angle (°)
≤20
≥65
d
Current dyke tip depth / dyke height (km)
Dyke current upper tip depth
Dyke current lower tip depth
Dyke height
Graben half-width / dyke tip depth below HF (m)
Dyke upper tip depth below HF
Graben half-width at HF
Maximum heave / apparent dyke thicknes (m)
Apparent dyke thickness
Cumulative maximum heave
F1 maximum heave
F2 maximum heave
Distance (km)
e
Dyke upper tip depth below HF (m)
Graben half-width at HF (m)
1:1
R^2 = 0.13
f
F1 and F2 average dip (°)
Graben half-width at HF (m)
R^2 = 0.37
g
(i)
(ii)
(iii)
Displacement (m)
Depth (km)
HK
HI
HA
+10%
-10%
L.o.S
L.o.V

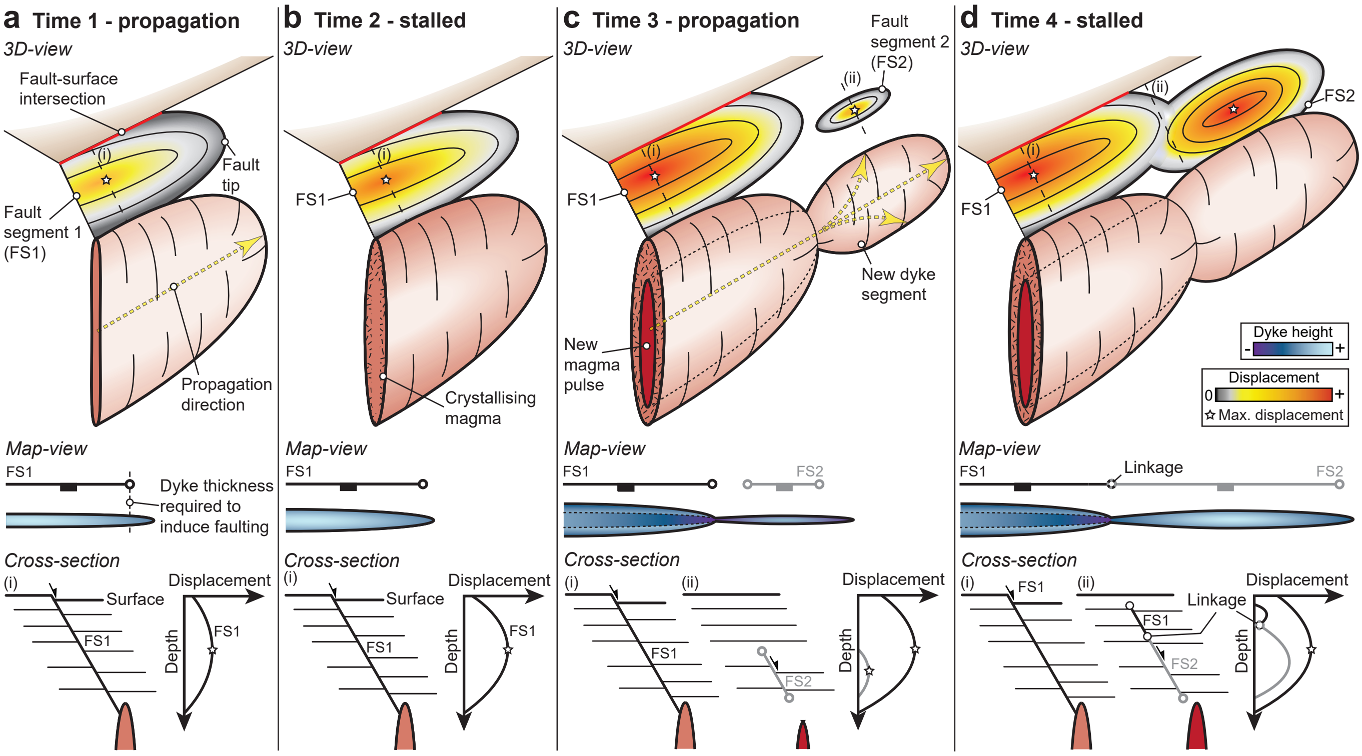

a Time 1 - propagation
3D-view
Fault-surface intersection
(i)
Fault tip
Fault segment 1 (FS1)
Propagation direction
Map-view
FS1
Dyke thickness required to induce faulting
Cross-section
(i)
Surface
FS1
Displacement
Depth
FS1
b Time 2 - stalled
3D-view
(i)
FS1
Crystallising magma
Map-view
FS1
Cross-section
(i)
Surface
FS1
Displacement
Depth
FS1
c Time 3 - propagation
3D-view
(i)
Fault segment 2 (FS2)
(ii)
FS1
New dyke segment
New magma pulse
Map-view
FS1
FS2
Cross-section
(i)
(ii)
FS1
FS2
Displacement
Depth
d Time 4 - stalled
3D-view
(i)
(ii)
FS2
FS1
Dyke height
-
+
Displacement
0
+
Max. displacement
Map-view
FS1
Linkage
FS2
Cross-section
(i)
FS1
(ii)
FS1
Linkage
FS2
Displacement
Depth

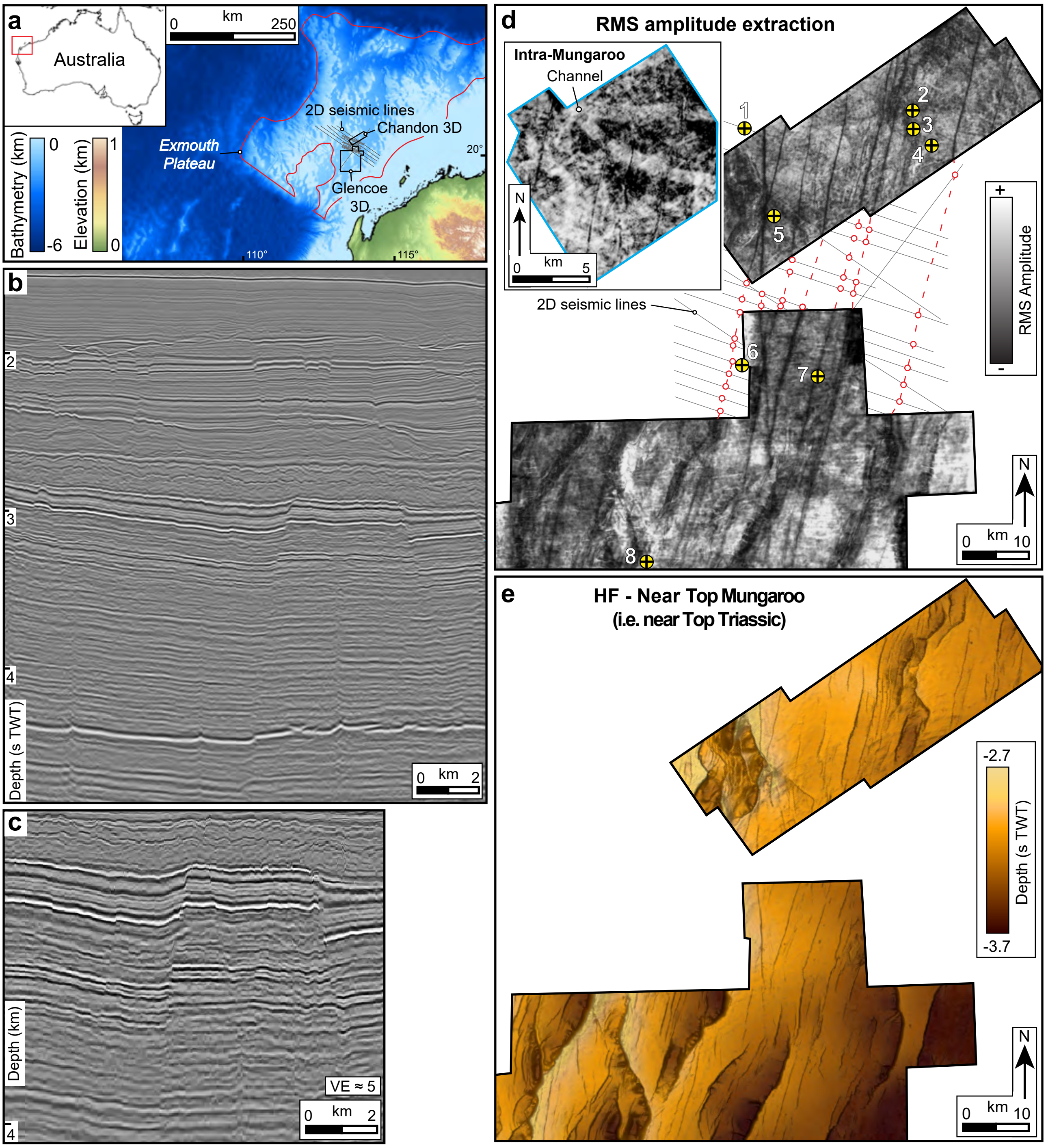

a
Australia
km
0
250
Bathymetry (km)
0
-6
Elevation (km)
1
0
Exmouth Plateau
2D seismic lines
Chandon 3D
Glencoe 3D
20°
110°
115°
b
2
3
4
Depth (s TWT)
0 km 2
c
Depth (km)
4
VE ≈ 5
0 km 2
d
RMS amplitude extraction
Intra-Mungaroo
Channel
N
0 km 5
2D seismic lines
1
2
3
4
5
6
7
8
+
-
RMS Amplitude
N
0 km 10
e
HF - Near Top Mungaroo
(i.e. near Top Triassic)
-2.7
-3.7
Depth (s TWT)
N
0 km 10